Mon. Not. R. Astron. Soc. **000**, 1–9 (2006) Printed 17 January 2008 (MN LATEX style file v2.2)

Is Ursa Major II the Progenitor of the Orphan Stream?

M. Fellhauer[1] ⋆, N.W. Evans[1], V. Belokurov[1], D.B. Zucker[1], B. Yanny[2], M.I. Wilkinson[1], G. Gilmore[1], M.J. Irwin[1], D.M. Bramich[1], S. Vidrih[1], P. Hewett[1], T. Beers[3]

[1] *Institute of Astronomy, University of Cambridge, Madingley Road, Cambridge CB3 0HA, UK*
[2] *Fermi National Accelerator Laboratory, P.O. Box 500, Batavia, IL 60510, USA*
[3] *Department of Physics and Astronomy and Joint Institute for Nuclear Astrophysics, Michigan State University, East Lansing, MI 48824, USA*

17 January 2008

ABSTRACT

Prominent in the 'Field of Streams' – the Sloan Digital Sky Survey map of substructure in the Galactic halo – is an 'Orphan Stream' without obvious progenitor. In this numerical study, we show a possible connection between the newly found dwarf satellite Ursa Major II (UMa II) and the Orphan Stream. We provide numerical simulations of the disruption of UMa II that match the observational data on the position, distance and morphology of the Orphan Stream. We predict the radial velocity of UMa II as $-100\,\mathrm{km\,s^{-1}}$, as well as the existence of strong velocity gradients along the Orphan Stream. The velocity dispersion of UMa II is expected to be high, though this can be caused both by a high dark matter content or by the presence of unbound stars in a disrupted remnant. However, the existence of a gradient in the mean radial velocity across UMa II provides a clear-cut distinction between these possibilities. The simulations support the idea that some of the anomalous, young halo globular clusters like Palomar 1 or Arp 2 or Ruprecht 106 may be physically associated with the Orphan Stream.

Key words: galaxies: dwarfs — galaxies: individual: UMa II — galaxies: kinematics and dynamics — galaxies: evolution — methods: N-body simulations

1 INTRODUCTION

Data from the Sloan Digital Sky Survey (SDSS; York et al. 2000) have revealed abundant examples of streams and substructure in the Milky Way halo. For example, Belokurov et al. (2006a) used a simple colour cut $g - r < 0.4$ to map out the distribution of stars in SDSS Data Release 5 (DR5). The "Field of Streams", an RGB-composite image composed of magnitude slices of the stellar density of these stars, showed the leading arm of the well-known Sagittarius stream and the Monoceros ring very clearly. Also prominent was a new stream, which did not have an identified progenitor, and was called the Orphan Stream by Belokurov et al. (2006a).

The Orphan Stream was then analysed independently by two groups. Grillmair (2006) reported that there was a diminutive Galactic satellite that lay near the projected path of the new stream but that it was "unlikely to be related to it". Belokurov et al. (2006b) disagreed, noting that the diminutive satellite lay on the same Galactocentric great circle as the Orphan Stream. They argued that there was a preponderance of unusual objects along this great circle – including the Complex A High Velocity Clouds and the young halo globular clusters Ruprecht 106 and Palomar 1 – and suggested that some or all may be the remnants of the disruption of a dwarf galaxy. Then, Zucker et al. (2006) provided follow-up Subaru imaging of the diminutive satellite, confirming it as a disrupted dwarf galaxy and naming it Ursa Major II (UMa II) after its host constellation.

One possible interpretation of the data is that UMa II is the progenitor of the Orphan Stream. Closely related is the possibility that both UMa II and the Orphan Stream are remnants from the break-up of a still larger object, perhaps a tidal dwarf galaxy (see e.g., Kroupa 1997). In this theoretical study, we strengthen the case for such interpretations by providing an orbit for the disruption of UMa II so that its tidal tails match the observational data available on the Orphan Stream.

2 OBSERVATIONAL DATA

The UMa II dwarf galaxy (Zucker et al. 2006) is located at right ascension $\alpha = 132.8^\circ$ and declination $\delta = +63.1^\circ$. Its heliocentric distance is estimated as $D_\odot = 30 \pm 5\,\mathrm{kpc}$, whilst its radial velocity is as yet unmeasured. UMa II appears elongated along lines of increasing right ascension with an ellipticity of ~ 0.5. Follow-up observations of the central parts with Subaru reveal more than one density enhancement within the satellite, which supports the fact that it may be in the process of tidal disruption. But, no obvious tails around the object are discernible in the wider field SDSS data.

⋆ Email: madf@ast.cam.ac.uk,nwe@ast.cam.ac.uk,vasily@ast.cam.ac.uk

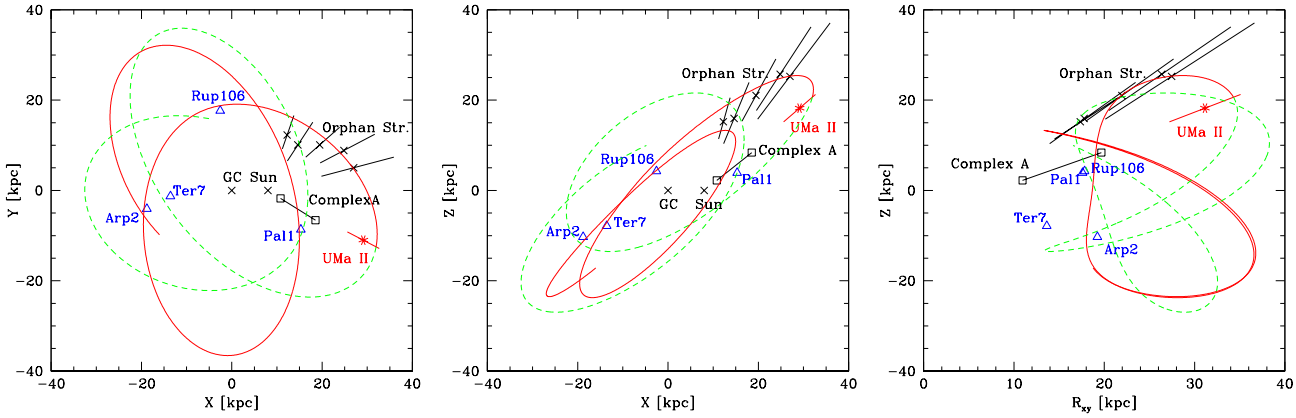

Figure 1. Orbit of UMa II in the (x, y)-plane (left), (x, z)-plane (middle) and $(R = \sqrt{x^2 + y^2}, z)$-plane (right). The red solid line is the backwards orbit from the present position and the green dashed line is the forward orbit over 1.5 Gyr. The red star with error bar shows the present position of the UMa II dwarf galaxy. Black crosses with error bars show the position of the Orphan Stream from Table 1. The positions of some globular clusters which may be associated with the stream are marked with blue, open triangles. The distance bracket to the Complex A is marked with black, open squares.

Table 1. Positions, distance moduli, distances and heliocentric velocities of the Orphan Stream From Belokurov et al. (2006b).

α	δ	$m - M$	$D_\odot$	$v_\odot$
$162.1°$	$-0.5°$	16.5 ± 0.7	20^{+7}_{-5} kpc	-35 ± 10 km s^{-1}
$158.9°$	$8.5°$	16.5 ± 0.9	20^{+10}_{-7} kpc	—
$155.4°$	$17.0°$	17.1 ± 0.7	26^{+10}_{-7} kpc	—
$152.3°$	$25.0°$	17.5 ± 0.8	32^{+13}_{-10} kpc	—
$149.4°$	$32.0°$	17.5 ± 0.9	32^{+15}_{-12} kpc	$+105 \pm 10$ km s^{-1}

The total luminosity of UMa II is $M_{\mathrm{tot,V}} = -3.8 \pm 0.6$ mag. This translates into a stellar mass of $\approx 6 \times 10^3$ M$_\odot$, applying a conservative mass-to-light ratio of 2 which is typical for an old population. This is a lower limit for the present-day mass of the remnant object.

UMa II lies on the same great circle as the Orphan Stream. This can be traced for over $\sim 50°$ in upper main sequence and turn-off stars in the SDSS data. By constructing a colour-magnitude mask based on the ridge-line of the old metal-poor globular cluster M92, Belokurov et al. (2006b) showed that the Orphan Stream is closer to us at lower declinations than at higher. The distances and distance moduli to the Stream at different right ascension and declination are listed in Table 1.

The total magnitude of the Orphan Stream is $m_r \approx 9.8$. Assuming the smallest distance modulus from Table 1 of $m - M = 16.5$, this results in $M_r \sim -6.7$ or 3.5×10^4 solar luminosities. Taking the largest distance modulus of $m - M = 17.5$, the total luminosity of the stream is $\approx 8 \times 10^4$ L$_\odot$. With a mass-to-light ratio for an old stellar population of 2, this amounts to a total mass in stars in the Orphan Stream of $\approx 10^5$ M$_\odot$.

Belokurov et al. (2006b) speculated that there might be a connection between the Orphan Stream and the agglomeration of high velocity clouds known as Complex A, which lie on the same great circle. Complex A is located between $\alpha = 126.7°$, $\delta = 67.4°$ and $\alpha = 134.5°$, $\delta = 61.7°$ with a distance bracket between 4 and 15 kpc in heliocentric distance (see e.g., Wakker et al. 1996; Wakker 2001). The measured radial velocity of this cloud complex is in the range of -140 to -190 km s^{-1}. Of course, the velocities of gas clouds may be affected by forces other than gravitational ones.

3 SET-UP

Our working hypothesis is that the UMa II dwarf galaxy is the progenitor of the Orphan Stream. To determine a possible orbit, we first perform test-particle integrations in a Milky Way potential which consists of a logarithmic halo of the form

$$\Phi_{\mathrm{halo}}(r) = \frac{v_0^2}{2} \ln\left(x^2 + y^2 q^{-2} + d^2\right), \quad (1)$$

with $q = 1, v_0 = 186$ km s^{-1} and $d = 12$ kpc. The disc is represented by a Miyamoto-Nagai potential:

$$\Phi_{\mathrm{disc}}(R, z) = \frac{GM_{\mathrm{d}}}{\sqrt{R^2 + \left(b + \sqrt{z^2 + c^2}\right)^2}}, \quad (2)$$

with $M_{\mathrm{d}} = 10^{11}$ M$_\odot$, $b = 6.5$ kpc and $c = 0.26$ kpc. Finally, the bulge is modelled as a Hernquist potential

$$\Phi_{\mathrm{bulge}}(r) = \frac{GM_{\mathrm{b}}}{r + a}, \quad (3)$$

using $M_{\mathrm{b}} = 3.4 \times 10^{10}$ M$_\odot$ and $a = 0.7$ kpc. The superposition of these components gives quite a good representation of the Milky Way. The circular speed at the solar radius is ~ 220 km s^{-1}. The major advantage is the analytical accessibility of all quantities (forces, densities, and so on).

First, we use trial and error to find a suitable orbit which reproduces most of the observational data. We then compute this orbit backwards for 10 Gyr and insert a live progenitor. We use the particle-mesh code Superbox (Fellhauer et al. 2000) to perform the forward integration until the position of UMa II today is reached. We then analyse the location of the tidal tails, adjust the parameters from the test-particle simulation and re-run the full N-body model to optimise the fit to the observational data. This procedure has to be done because the location of the tidal tails differs from that of the orbit.

At outset, we do not distinguish between dark and luminous matter and use a one-component model with a Plummer profile. Later, we also use a more elaborate two-component model, motivated by the endpoints of cosmological simulations. It has a Hernquist sphere corresponding to the luminous matter, embedded in a dark matter halo which has the Navarro-Frenk-White form. We in-

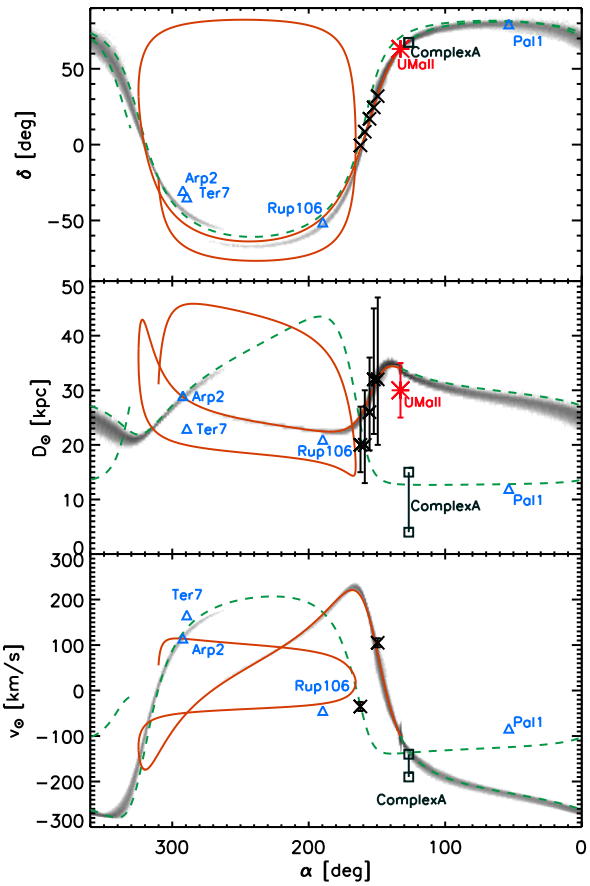

Figure 2. All-sky view of the UMa II orbit and the best matching simulation. The panels show right ascension versus declination (upper), right ascension versus heliocentric distance (middle) and right ascension versus heliocentric radial velocity (lower). The grey-scale contours show the logarithmic densities of the UMa II tidal tails in the simulation. The solid red (dashed green) line is the backward (forward) orbit shown for 1.5 Gyr. Black crosses mark the position of the Orphan Stream and the red star marks the position of UMa II. Blue triangles show the globular clusters, Arp 2, Terzan 7, Ruprecht 106 and Palomar 1. Squares show the position of Complex A with its distance and velocity brackets. [The starting mass of the Plummer model representing UMa II is 4×10^5 M$_\odot$ and its scale-length is 80 pc]

vestigate the effects of changing the initial mass, dark matter content and scale-lengths of both models.

4 THE ORBIT

4.1 Predicted Velocities

Our best matching orbit puts UMa II at a heliocentric distance of 34 kpc, which agrees with the observational datum of Zucker et al. (2006). We predict the radial velocity and (heliocentric) proper motions of UMa II as

$$\begin{aligned} v_\odot &= -100\,\mathrm{km\,s^{-1}}, \\ \mu_\alpha \cos\delta &= -0.33\ \mathrm{mas\ yr^{-1}} \\ \mu_\delta &= -0.51\ \mathrm{mas\ yr^{-1}}. \end{aligned} \quad (4)$$

The resulting orbit is shown in Fig. 1. It has a perigalacticon of ~ 18.4 kpc and an apogalacticon of ~ 40.6 kpc. This orbit not only connects UMa II with the Orphan Stream but also permits Complex A and several globular clusters of the Milky Way to be related to it.

The tidal tails of UMa II do not lie precisely along UMa II's orbit. Fig. 2 shows grey-scale contours of the tidal debris in the planes of right ascension versus declination, heliocentric distance and heliocentric velocity respectively. The positional data on the Orphan Stream is nicely matched by the tidal tails. The model predicts a strong velocity gradient along the Orphan Stream with the radial velocity varying from 200 kms^{-1} at the southern end ($\alpha \approx 170°$) to -100 kms^{-1} at the northern end ($\alpha \approx 130°$). The gradient in radial velocity becomes shallower at higher declinations.

The Orphan Stream may also have been detected as a density enhancement in star count data derived from CADIS or the Calar Alto Deep Imaging Survey (Fuchs et al. 2006). This idea receives some support from Fig. 2, as their 9h field falls on the second wrap of the backward orbit.

4.2 Possibly Associated Objects

On the basis of intersections of their polar paths, Belokurov et al. (2006b) speculated that there may be a connection between the Orphan Stream and a number of anomalous, young halo globular clusters – in particular Palomar 1, Ruprecht 106, Arp 2 and Terzan 7.

From Figs. 1 and 2, we can assess how Belokurov et al.'s speculations fare against the simulation. The position and radial velocity of Pal 1 is a good match to the forward orbit of UMa II. In this context, it is interesting to note that Figure 1 of Zucker et al. (2006) shows clumps visible in the central parts of UMa II. Pal 1 looks like one such clump that has already broken off and leads UMa II. Arp 2 is also well-matched in position and radial velocity of the forward orbit, although it has also been claimed as a possible Sagittarius stream member on the basis of distance, kinematics and chemical composition (see e.g., Sbordone et al. 2005). The position of Rup 106 is a good match to the backwards orbit, but its velocity is not (it should lie on the upper rather than the lower wrap in Fig. 2). However, bearing in mind the distance errors to the globular clusters, Rup 106 probably cannot be discarded. Ter 7 does seem to be ruled out – the right panel of Fig. 1 and the middle panel of Fig. 2 show substantial mismatches between its distance and that of the forward orbit of UMa II.

Belokurov et al. (2006b) also pointed out the remarkable alignment between the Orphan Stream and the Complex A association of High Velocity Clouds (HVCs). Although we do not address the origin of Complex A in this paper, we note that the forward orbit does pass through the location of Complex A, and even the heliocentric velocities are reasonably well-matched (see the lower panel of Fig. 2). If the clouds of Complex A are indeed associated with the Orphan Stream, the simulation suggests that they lie more than a revolution ahead in orbital phase.

5 THE MORPHOLOGY OF THE ORPHAN STREAM

With this orbit in hand, we can deduce some constraints on the initial mass of UMa II. The length of the tidal tails is controlled by the total initial mass of the satellite (dark and luminous matter are of

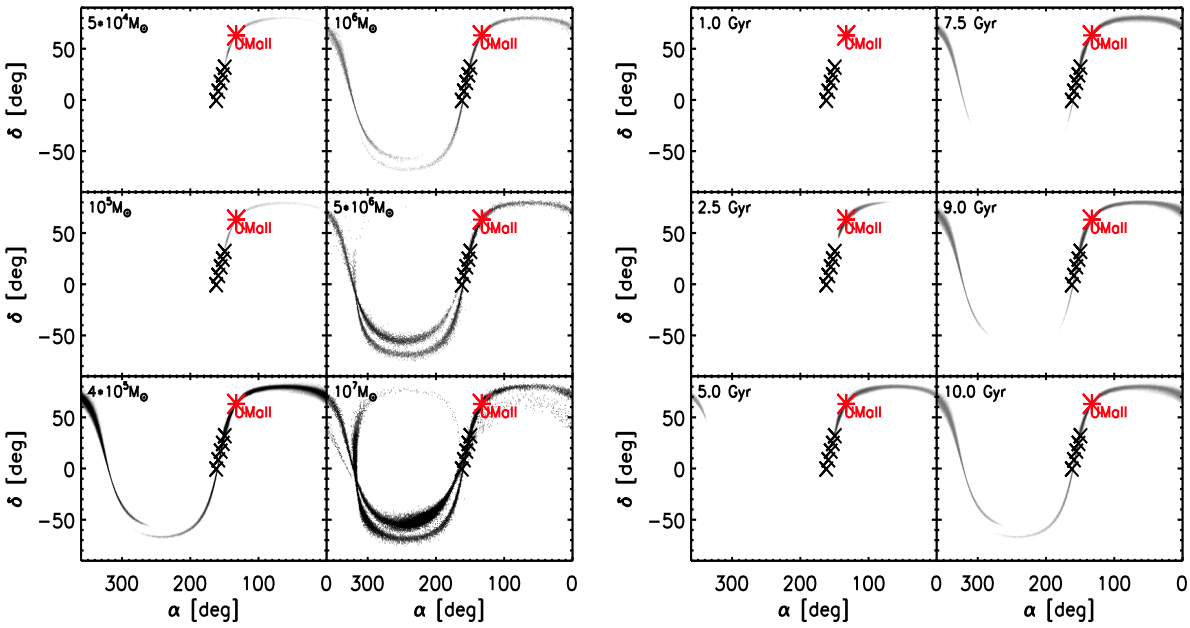

Figure 3. Left: The length of the tidal tail as a function of the initial mass of the object, shown in the top left of each panel. The red star shows the position of UMa II, the black crosses the positions of the Orphan Stream. If the initial mass is of the order 5×10^6 $M_\odot$ or more, we should see more than one wrap. If the initial mass is of the order 10^5 $M_\odot$ or less, the tail is not long enough to match the Orphan Stream. [The scale-length of the Plummer model representing the progenitor of UMa II is 80 pc. The duration of the simulation is 10 Gyr.] Right: The length of the tidal tails as a function of time, shown in the top left of each panel. The time has to be on the order of 7.5 Gyr or greater to ensure that the tails are long enough to match the Orphan Stream. [The starting mass of UMa II is 4×10^5 $M_\odot$ and its scale-length is 80 pc.]

course not differentiated in our one-component simulations). If this mass is $\lesssim 10^5$ $M_\odot$, the resulting tails are too short to be consistent with the $\sim 50^\circ$ arc of the Orphan Stream visible in SDSS. On the other hand, if the initial mass is $\gtrsim 5 \times 10^6$ $M_\odot$, further wraps of the leading and trailing arms should then be seen in SDSS data. This is illustrated in the left panels of Fig. 3, which shows the tidal tails produced by the disruption of a sequence of UMa IIs of different starting masses. Similarly, sequences of the disruption of UMa IIs for different times, as shown in the right panels of Fig. 3, suggest that timescales less than 7.5 Gyr are insufficient to reproduce the present-day length of the Orphan Stream.

Having found lower limits for the progenitor mass and the simulation time, we now focus on two particular models. The first is a one-component model in which dark and luminous matter are not distinguished. It has a Plummer distribution with a mass of $M_{\rm pl} = 4 \times 10^5$ $M_\odot$ and a scale-length of $R_{\rm pl} = 80$ pc. The rationale for these parameters will become clear in Sect. 6, where we place further constraints on the progenitor mass by investigating the remnant. The second is a two-component model with the luminous matter represented by a Hernquist sphere with mass $M_{\rm hern} = 5 \times 10^5$ $M_\odot$ and a scale-length of 200 pc. The is embedded in a Navarro-Frenk-White (NFW) dark matter halo. The NFW model has the same scale-length as the luminous matter, together with a mass within the cut-off radius (set to be the tidal radius at perigalacticon) which is ten times greater than the luminous mass. If the NFW mass is made larger or the scale-length smaller, then the progenitor becomes much harder to disrupt and does not resemble the present-day UMa II.

Fig. 4 shows a close-up of the simulation data at the position of the Orphan Stream for the one and two-component models. There are a number of morphological features that both the simulations reproduce successfully. First, the tidal tails of the models have a full-width half-maximum (FWHM) of $\sim 2^\circ$. This matches the FWHM of the Orphan Stream as measured by Belokurov et al. (2006b). In both simulations, the mass in the Orphan Stream is $\lesssim 10^5$ $M_\odot$, in reasonable agreement with the stellar mass inferred from its luminosity of $\sim 8 \times 10^4 L_\odot$ (Belokurov et al. 2006b). There is just one arm visible in the one-component model, and the total mass in the Stream is $\sim 6 \times 10^4$ $M_\odot$. This is a closer match than the $\sim 3 \times 10^4$ $M_\odot$ in stars present in both arms in the Orphan Stream for the two-component model.

Both models reproduce the positional data of the Orphan Stream very well and are in good agreement with the measured distances. Nevertheless, in the two-component model, a wrap-around of the leading arm is present, which gives a better fit to the two low declination data points in the middle panels of Fig. 4. Further, the velocity data-point at the low declination (or high right ascension) end of the Stream shown in the lower panels of Fig. 4 can only be reproduced with the presence of a wrapped around leading arm.

6 THE MORPHOLOGY OF UMA II

We can sharpen the constraints on the initial mass by requiring that the simulations also reproduce the disrupted nature of UMa II itself. Fig. 5 shows the results of the disruption of the one-component model (left panels) and the two-component model (right panels). The three rows show the surface brightness, the logarithmic density distribution in right ascension-heliocentric distance and in right ascension-heliocentric velocity space, respectively.

For one-component models, we find that satellites with an

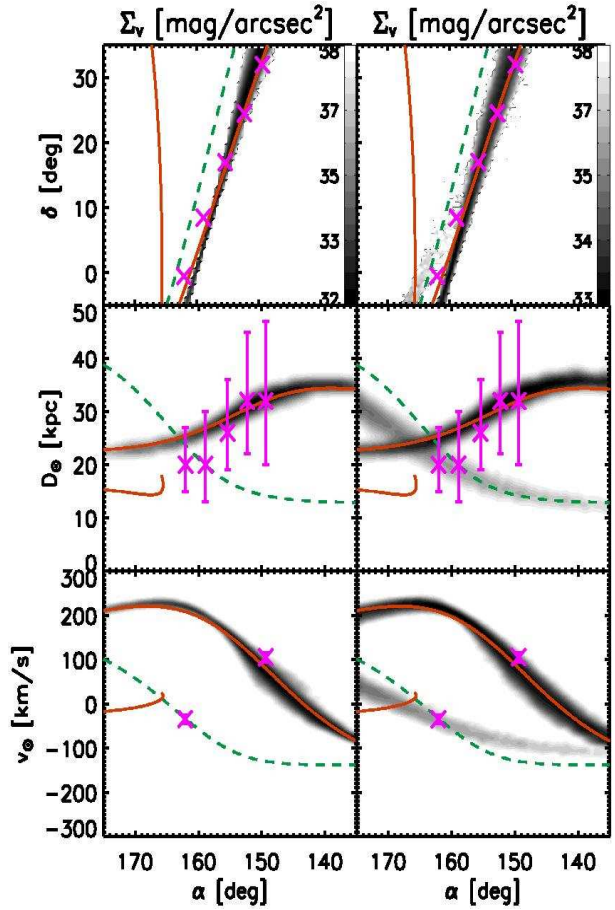

Figure 4. A close-up of the Orphan Stream in the one-component model (left panels) and the two-component model, showing luminous mass only (right panels). Red solid (green dashed) line shows the backward (forward) orbit of UMa II. The purple crosses with error-bars mark the observational results from Belokurov et al. (2006b). From top to bottom the panels show the surface brightness in V (mass is converted into luminosity using a mass-to-light ratio of 2), the logarithmic density distribution in right ascension–heliocentric distance space and the logarithmic density distribution in right ascension–radial velocity space. Both models match the positional data of the Orphan Stream. Both models also fit the observational distances within the errors, but in the two-component model the closest two data-points are better matched with the wrap-around of the leading arm, which is not present in the one-component model. Also, the velocity measurements are only matched if the leading arm is present.

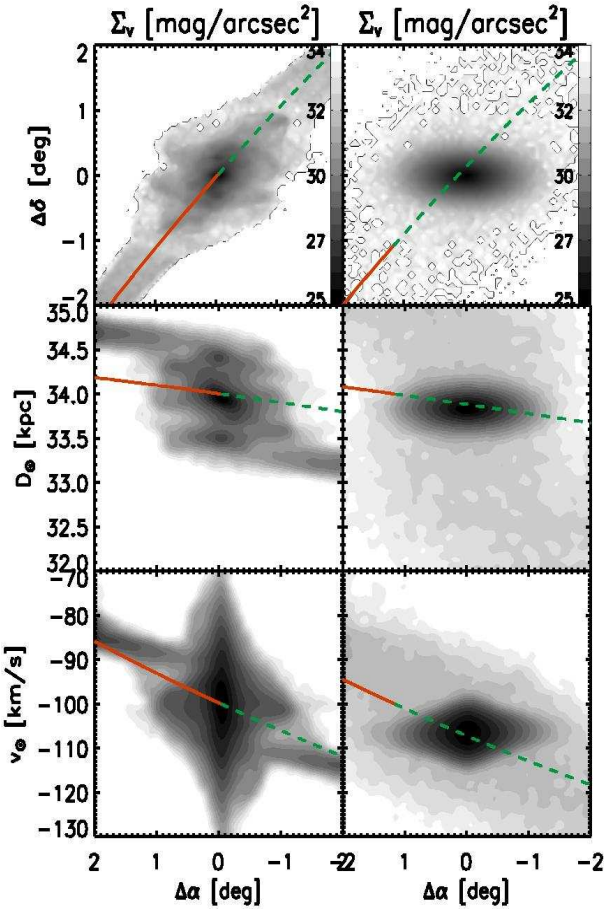

Figure 5. A close-up of the UMa II remnant in both models. Left panels show again the one-component model, while right panels show the two-component model. The top row shows the surface brightness of all particles in the one-component model and of the luminous matter only in the two-component model. The second row gives the logarithmic density distribution in right ascension–distance space while the third row shows the distributions in right ascension–radial velocity. The coloured lines are as in Fig. 4.

initial mass $\gtrsim 10^6$ M$_\odot$ do not become sufficiently dissolved to resemble the present-day UMa II. Below this, there is a trade-off between starting mass and scale-length. For example, a Plummer sphere with mass $M_{\rm pl} = 5 \times 10^5$ M$_\odot$ and scale-length $R_{\rm pl} = 100$ pc gets completely dissolved without a remnant, whilst one with $R_{\rm pl} = 85$ pc gives a remnant which is too massive by two orders of magnitude. Reducing the mass to $M_{\rm pl} = 4 \times 10^5$ M$_\odot$ and using $R_{\rm pl} = 80$ pc results in a remnant with similar mass and aspect to UMa II. Fig. 6 shows the evolution of the bound mass of our one-component model. If the final mass of the remnant is $\sim 6 \times 10^3$ M$_\odot$, then an object with an initial mass of $\sim 10^5$ M$_\odot$ must be in its final stage of dissolution. A robust result is that the initial distribution of the satellite cannot be very concentrated, otherwise there is insufficient mass loss to produce the Orphan Stream.

For two-component models, it is a challenge to reproduce the dissolved nature of the present-day UMa II. As our illustrative ex-

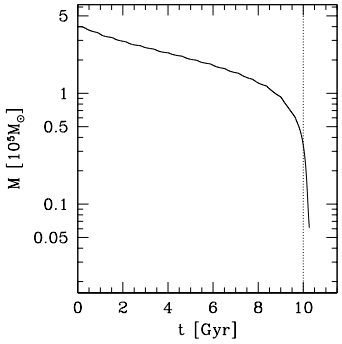

Figure 6. The bound mass of UMa II is plotted against time for the one-component model. During most of its lifetime, the mass decreases only slightly with each perigalacticon passage. However, the last disc shock leads to the final disruption of the object and the bound mass drops quickly to zero. At this particular instant, the stars of the object become unbound but have not yet dispersed from the location of the object. At later epochs, the bound mass is zero and the stars disperse into the tails.

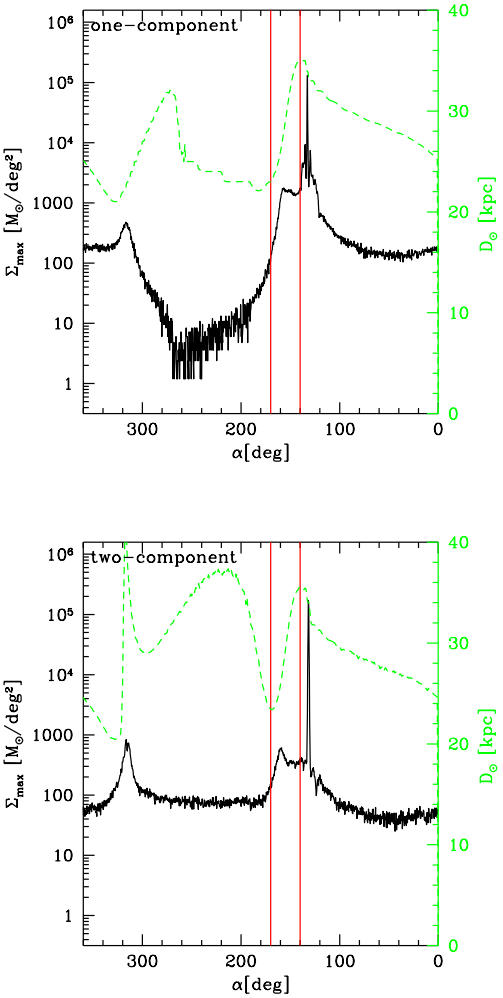

Figure 7. The peak surface density $\Sigma_{\rm max}$ (black) and the mean heliocentric distance $D_\odot$ (green) of the Orphan Stream are plotted as a function of right ascension for the one-component (two-component) models in the upper (lower) panels. The vertical red lines mark the range of right ascension over which the Orphan Stream is detected in SDSS data. UMa II corresponds to the sharp density peak at right ascension $\alpha = 132.8°$. The fading of the Orphan Stream just before it approaches UMa II is caused by the decreasing peak surface density and the increasing mean distance.

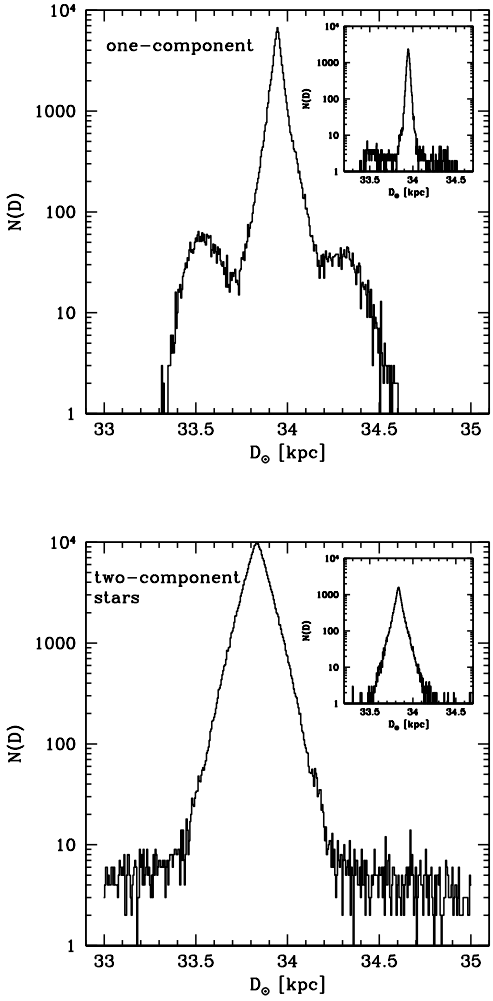

Figure 8. Histogram of heliocentric distances of stars in a $0.4° \times 0.4°$ field centred on UMa II, approximately the same size as the panels in Zucker et al. (2006). The inset shows the histogram of distances but now confined to the very central parts of UMa II ($0.1° \times 0.1°$ field). The data are taken from the one-component (two-component) model in the upper (lower) panels.

ample, we use a Hernquist sphere of 5×10^5 M$_\odot$ and scale-length of 200 pc, embedded in a Navarro-Frenk-White halo with the same scale-length and with a mass of 5×10^6 M$_\odot$ within the tidal radius of 400 pc. These parameters are set given the constraint that the present-day mass in the Orphan Stream is $\sim 10^5$ M$_\odot$. If the mass-to-light ratio of the progenitor is $\sim$ 10, this fixes the halo mass, whilst the scale-lengths must be in excess of 200 pc to allow for enough luminous matter to be stripped off and found in the Orphan Stream. Even so, at the endpoint of the simulation, the remnant has $\sim 10^5$ M$_\odot$ in stars. This is too large by two orders of magnitude!

For both the one and two component models, the UMa II remnant in Fig. 5 shows a prominent elongation – not along its orbit – but along lines of constant declination. The same elongation is found in the deeper, follow-up observations with the Subaru telescope reported by Zucker et al. (2006). Comparing the size of the observed UMa II of about one degree along constant declination with our models, we conclude that our one-component model fits the extension of the real object much better than the two-component model.

Another advantage of the one-component model is that there is some substructure in the UMa II remnant, as is visible in the upper left panel of Fig. 5. In the simulation, this is caused by tidal shocking of the remnant at the last few disk passages. The substructure is qualitatively similar to internal clumpiness of the UMa II dSph seen by Zucker et al. (2006). However, to recover the details of this feature may well require a more elaborate starting model than a simple Plummer sphere. The two-component model shows no substructure at the end of the simulation.

Both simulations not only match all the available positional data, but – more strikingly – they also explain why the tails around UMa II are faint and undetectable with SDSS. At the positions of the Orphan Stream, projection effects enhance the visibility of the well-collimated stream, which lies almost along the line of sight. By contrast, at UMa II the orbit is almost transverse to the line

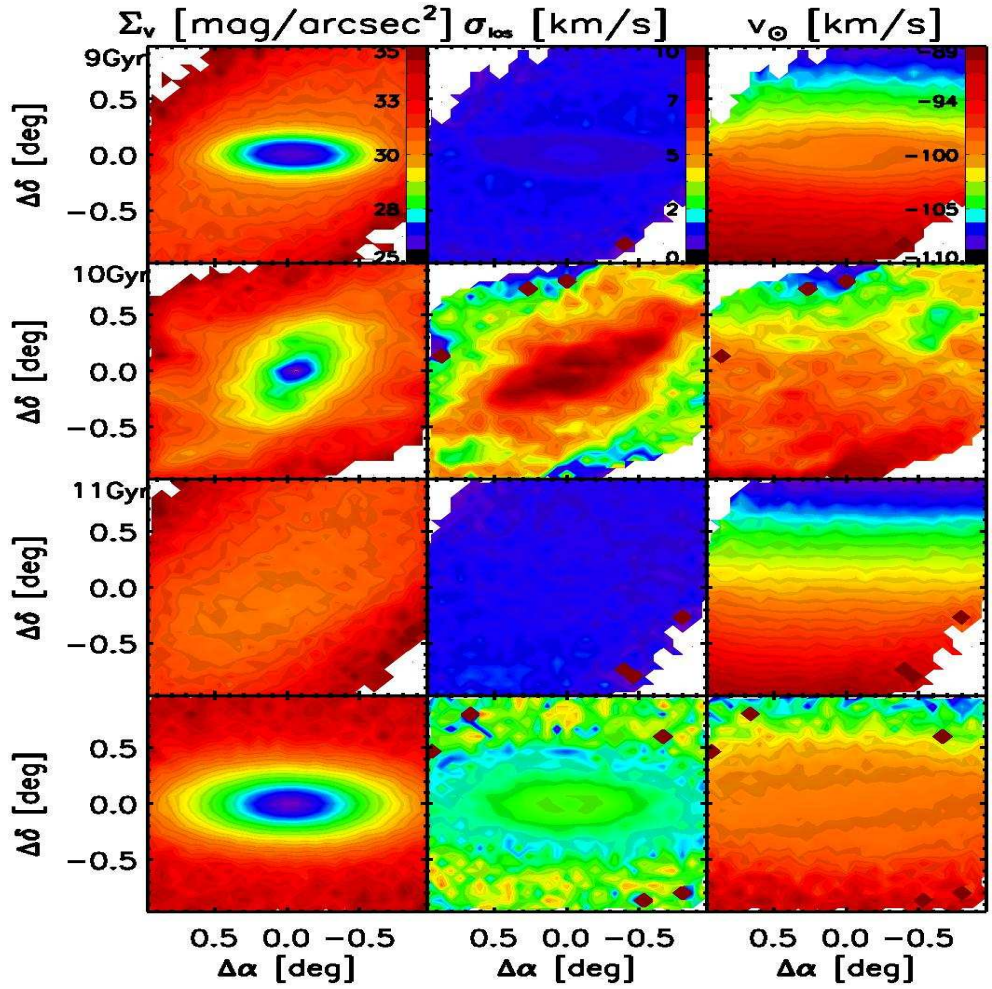

Figure 9. This shows contours of the V band surface brightness, the velocity dispersion and the mean radial velocity of the remnant in our simulations. The first three rows refer to the one-component model after 9 Gyr, 10 Gyr and 11 Gyr. This is a sequence from bound through disrupting to almost completely dissolved object. The final row shows the endpoint of the two-component model after 10 Gyr for comparison. (The key to the colour code is given on the right-side of the top panels).

Galactic Model	q	$D_\odot$ [kpc]	$v_\odot$ [km s^{-1}]	μ_α [mas yr^{-1}]	μ_δ [mas yr^{-1}]	$R_{\rm p}$ [kpc]	$R_{\rm a}$ [kpc]
Miyamoto-Nagai disc, Logarithmic halo	0.90	30	-100	-0.50	-0.50	18.9	34.5
Miyamoto-Nagai disc, Logarithmic halo	1.00	30	-115	-0.40	-0.50	18.8	37.2
Miyamoto-Nagai disc, Logarithmic halo	1.11	30	-105	-0.35	-0.50	17.8	36.7
Dehnen & Binney models	1.00	33	-125	-0.25	-0.65	14.2	40.8

Table 2. Parameters for best fit test-particle orbits for different choices of potential. The first column gives the Galactic model. For the logarithmic halos, q is the flattening of the equipotentials [see eq. (1)], whereas for the Dehnen & Binney (1998) models, q is the flattening of the isodensity contours [see eq (5)]. The columns give the best-fit initial conditions of UMa II today so as to join up with the Orphan Streaml; the heliocentric distance, heliocentric radial velocity and proper motion in α and δ. The last two columns show the peri- and apogalacticon distances of the orbit. Note that the values for the $q = 1$ logarithmic halo case differ slightly from the values in the main paper because only the test-particle orbit was fit to the data in this Table.

of sight and there is no enhancement from projection effects. This provides a natural explanation as to why an extension of the Orphan Stream is not visible all the way up to the position of UMa II in SDSS data. This phenomenon is also illustrated in Fig. 7 which shows the peak density in the simulated Orphan Stream dropping, and the mean heliocentric distance increasing, as UMa II is approached.

Fig. 8 shows the distribution of heliocentric distances of stars in a $0.4^\circ \times 0.4^\circ$ field centred on UMa II remnant, together with an inset that records the same information but now confined to the very innermost $0.1^\circ \times 0.1^\circ$ field. Although the innermost parts are quite confined, the entire object has a significant depth along the line of sight of ~ 1 kpc, particularly in the one-component model. This is

of the right order of magnitude to cause the broadening of features of the colour-magnitude diagram discerned by Zucker et al. (2006).

7 VELOCITY DISPERSIONS

We have shown that the initial mass (stars and possible dark matter) must exceed 10^5 $M_\odot$ to account for the length of the tidal tails and the known stellar mass in the Orphan Stream. But any object with a total mass $> 10^6$ $M_\odot$ typically leads to a present-day UMa II which is still strongly bound and has a luminous matter contribution at least an order of magnitude larger than the observed 6×10^3 $M_\odot$.

One solution to this dilemma is to postulate that we are observing UMa II at a time close to its disintegration. The last disc passage led to the almost complete disruption of the remnant object. The stars are now rapidly becoming unbound. They have not yet dispersed along the orbit into the tidal tails and we still see them in the innermost parts of UMa II in a very confined area (see the inset of Fig. 7). If so, then the interpretation of kinematic data may need special care.

The first three rows of Fig. 9 all show one-component models. We used exactly the same set-up, but started the simulation at 9 Gyr, 10 Gyr or 11 Gyr ago on the same orbit to make sure all models are now seen at the same position on the sky (to exclude projection effects). The bound object in the first row has a small velocity dispersion, which is even lower than that in the surrounding tails. But the mean line of sight velocity is constant throughout the bound object and a gradient is only visible in the tails. This changes dramatically in the disrupting model shown in the middle panel. We still see an object with a similar total surface brightness, but it already shows sub-structure on small scales. The velocity dispersion is inflated by a factor of ten, but the dissolved nature of the remnant is already visible in the mean radial velocity. There is a strong gradient throughout the object, even though the mean velocity shows some flocculent structure. In the third row, in which the process of disruption is almost complete, the dissolved object has a low surface density, which will decrease further in the future until it matches that of the tails. The velocity dispersion is again low, at much the same value as that of the tails. Looking at the mean radial velocity, it is hard to distinguish what remains of the object from the tails. For comparison, the final row of Fig. 9 shows the same quantities for the two-component model. The final bound object has smooth surface brightness contours, a high velocity dispersion because of the dark matter content and no gradient in the mean radial velocity.

Follow-up high precision kinematic observations of this new dwarf galaxy could reveal a high velocity dispersion, irrespective of the dark matter content. However, the existence of a gradient in the mean radial velocity provides a clear-cut distinction between a disrupting object and a bound, dark matter dominated object.

8 THE GALACTIC POTENTIAL

Hitherto, our Galactic model is built from three fairly simple analytic components that could have some deficiencies. Although we are using the same standard model as many previous investigators (e.g., Helmi 2004; Johnston et al. 2005), it is prudent to examine the robustness of our results to changes in the underlying Galactic potential. Whilst re-running all the N-body simulations would be time-consuming, it is straightforward to carry out the initial test-particle calculations described in Section 2 for different potentials.

For example, we can vary the flattening of the halo. If we change the halo shape from spherical to moderately prolate or oblate, we still are able to fit all the data by slightly altering the starting velocities of UMa II. This is illustrated in Table 2, which gives the velocities, and the pericentric and apocentric distances for test particle calculations. Note that q in the logarithmic halo refers to the flattening of the equipotentials – the flattening in the density contours is typically two or three times greater (see e.g., Evans 1993). For moderate changes, a suitable orbit can always be found that joins up UMa II with the Orphan Stream, but UMa II's predicted velocity and proper motions are then somewhat different. Only if we use strongly prolate or oblate models does the orbit of UMa II change so dramatically that we are not able to fit all the data on the Orphan Stream at once. However, the recent study of the multiple wraps of the Sagittarius' stream by Fellhauer et al. (2006) provides strong evidence that only spherical or close to spherical halo shapes are possible for the Milky Way.

As a further check, we change the type of the Galactic potential and use a Dehnen & Binney (1998) model. These potentials consist of three exponential discs (thin, thick and gaseous). The halo and the bulge are represented by two spheroidal distributions

$$\rho_{\rm S}(R,z) \quad = \quad \rho_0 \left(\frac{m}{r_0}\right)^{-\gamma} \left(1+\frac{m}{r_0}\right)^{\gamma-\beta} \exp\left(-\frac{m^2}{r_{\rm t}^2}\right). \qquad (5)$$

Here $m^2 = R^2 + z^2 q^{-2}$ and q is the axis ratio in the density, whilst the remaining parameters are chosen as in Fellhauer et al. (2006). Table 2 shows how the intitial conditions or the test particle orbit change for the spherical case ($q = 1$) for comparison. Again, an orbit matching UMa II to the Orphan Stream can be found, and the changes in the initial conditions in Table 2 give an indication of the likely uncertainties in our predictions caused by changes in the Galactic potential.

9 CONCLUSIONS

We have carried out N-body simulations to model the evolution and disruption of the recently discovered dwarf galaxy UMa II. The simulations reproduce the available observational data on the Orphan Stream within their error margins. We conclude that UMa II is a likely progenitor of the Orphan Stream. We predict the radial velocity of UMa II as -100 km s^{-1}. We also predict a strong velocity gradient along the Orphan Stream with the radial velocity varying from ~ 200 kms^{-1} at the southern end to ~ -100 kms^{-1} at the northern end.

From the length of the tails and the mass found in the Orphan Stream, we deduce that the initial mass of UMa II is in excess of 10^5 $M_\odot$. But, an object more massive than 10^6 $M_\odot$ cannot be dissolved to produce the present day UMa II, at least on the orbit derived from the observations. Therefore, the initial mass of UMa II has to be of the order a few 10^5 $M_\odot$. To reduce UMa II's mass through tidal effects to its present value, the distribution of stars and dark matter has to be extended. We carried out a suite of simulations of the disruption of UMa II with one-component models, which have little dark matter beyond that associated with the stellar populations, and two-component models with a mass-to-light ratio of ~ 10. There are strengths and weaknesses of both sets of simulations. Both reproduce the positions and distances of the Orphan Stream, but the two-component models are in better agreement with the admittedly uncertain kinematic data derived by Belokurov et al. (2006b). However, the one-component models can provide a much

better match to the disrupted nature of UMa II today. The velocity dispersion is not a clean test between these two possibilities, as we have shown that objects undergoing disruption can have an anomalously high velocity dispersion. However, a clear-cut test is provided by the mean radial velocity, which should show no gradient for dark matter dominated models, but an obvious gradient for disrupting models.

The orbit that we have derived supports the idea of Belokurov et al. (2006b) that some of the anomalous, young halo globular clusters (particularly Pal 1, Arp 2 and possibly Rup 105) may be associated with the Orphan Stream. Intriguingly, the position and velocity of Complex A can also be matched, but only if it lies a revolution ahead in orbital phase. The association of these objects however makes most sense in the picture in which UMa II, the young halo globular clusters and Complex A are all fragments of a much larger object like a tidal dwarf galaxy.

ACKNOWLEDGMENTS

MF, VB, DBZ, MIW and DMB gratefully acknowledge financial support through PPARC. Funding for the SDSS and SDSS-II has been provided by the Alfred P. Sloan Foundation, the Participating Institutions, the National Science Foundation, the U.S. Department of Energy, the National Aeronautics and Space Administration, the Japanese Monbukagakusho, the Max Planck Society, and the Higher Education Funding Council for England. The SDSS Web Site is http://www.sdss.org/.

The SDSS is managed by the Astrophysical Research Consortium for the Participating Institutions. The Participating Institutions are the American Museum of Natural History, Astrophysical Institute Potsdam, University of Basel, Cambridge University, Case Western Reserve University, University of Chicago, Drexel University, Fermilab, the Institute for Advanced Study, the Japan Participation Group, Johns Hopkins University, the Joint Institute for Nuclear Astrophysics, the Kavli Institute for Particle Astrophysics and Cosmology, the Korean Scientist Group, the Chinese Academy of Sciences (LAMOST), Los Alamos National Laboratory, the Max-Planck-Institute for Astronomy (MPIA), the Max-Planck-Institute for Astrophysics (MPA), New Mexico State University, Ohio State University, University of Pittsburgh, University of Portsmouth, Princeton University, the United States Naval Observatory, and the University of Washington. MF, VB, DZ and MW thankfully acknowledge financial support through PPARC.

REFERENCES

Belokurov V., et al., 2006a, ApJ, 642, L137
Belokurov V., et al., 2006b, ApJ, in press (astro-ph/0605705)
Dehnen W., Binney J., 1998, MNRAS, 294, 429
Evans, N. W. 1993, MNRAS, 260, 191
Fellhauer M., Kroupa P., Baumgardt H., Bien R., Boily C.M., Spurzem R., Wassmer N., 2000, NewA, 5, 305
Fellhauer M., et al., 2006, ApJ, 651, 167
Fuchs B., Phleps S., Meisenheimer K., 2006, A&A, 457, 541
Grillmair, C., 2006, ApJ, 645, L37
Helmi, A. 2004, MNRAS, 351, 643
Johnston, K. V., Law, D. R., & Majewski, S. R. 2005, ApJ, 619, 800
Kroupa, P., 1997, New Astronomy, 2, 139
Sbordone L., Bonifacio P., Marconi G., Buonanno R., Zaggia S., 2005, A&A, 437, 905
Wakker, B., 2001, ApJS, 136, 463
Wakker B., Howk C., Schwarz, U., van Woerden, H., Beers, T., Wilhelm, R., Kalberla, P., Danly, L., 1996, ApJ, 473, 834
York D.G., et al., 2000, AJ, 120, 1579
Zucker D.B., et al., 2006, ApJ, 650, L41